Article

# Highly Selective $CO_2$ Separation on Na-exchanged DNL-6 Synthesized by Utilization of Spent Industrial Catalyst

TANG Yanling[1,2], WANG Quanyi[2], YAN NaNa[2], ZHANG Xiaosi[2,3], YANG Miao[2], TIAN Peng[2]✉ and LIU Zhongmin[2]✉

Received March 4, 2024
Accepted March 28, 2024


Conversion of industrial solid wastes into functional materials has attracted considerable interest, as it can reduce environmental pollution and facilitate the sustainable development of relevant processes. Herein, spent methanol-to-olefins (MTO) industrial catalyst was explored for the synthesis of DNL-6 molecular sieve, a promising SAPO-type adsorbent for $CO_2$ capture. It was demonstrated that DNL-6 with high purity and crystallinity, and various silica contents can be readily synthesized. Na-exchanged DNL-6 was further prepared using the as-synthesized DNL-6 as the precursor, and its structure was investigated by Rietveld refinement, revealing that Na cations were mainly located in the single 8-rings (S8Rs). Na-DNL-6 with varied silica contents and Na contents were investigated for adsorption studies. Na-DNL-6 with a high Na exchange degree exhibited comparable $CO_2$ uptake with H-DNL-6 (298 K and 101 kPa), but superior separation selectivity for $CO_2/CH_4$ (as high as 1369, 50/50 kPa) and $CO_2/N_2$ (∞, 15/85 kPa) owing to the "trapdoor" effect associated with the Na cations sited in the S8Rs. This work provides an eco-friendly approach for the synthesis of efficient silicoaluminophosphate adsorbent for $CO_2$ capture.

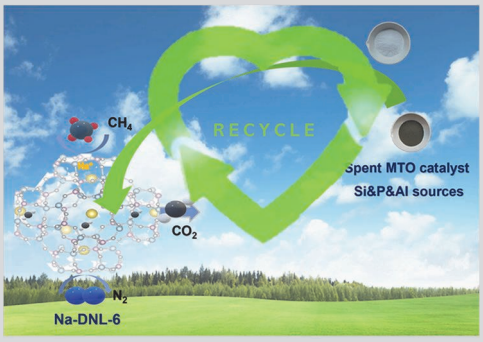


**Keywords** DNL-6; SAPO molecular sieve; Synthesis; $CO_2$ separation; Spent industrial catalyst

## 1 Introduction

Over the past decades, the increasing emissions of greenhouse gases, especially $CO_2$ generated by fossil combustion, have raised worrying problems of climate change.[1,2] The capture and separation of $CO_2$ from flue gases thus have received considerable attention.[3] Moreover, $CO_2$ separation from natural gas and biogas is also an important process, as contamination by $CO_2$ affects the transport and utilization of these gases.[4] The industrial technologies currently used for $CO_2$ capture are mainly based on aqueous amine absorption. This, however, suffers the drawbacks of high energy consumption for regeneration. Physical adsorption technologies, for example, pressure swing adsorption (PSA), have attracted great attention owing to the advantages of lower energy consumption and simple operation. A number of nanoporous materials have been extensively explored as adsorbents for selective separation of $CO_2/N_2$ and $CO_2/CH_4$, including microporous zeolites, porous carbon, metal-organic frameworks, porous organic polymers, etc.[4−12] Among them, zeotype materials, especially the small-pore zeolites showing a "molecular trapdoor" effect,[11,13,14] represent promising candidates when considering the factors determining the separation efficacy involving adsorption selectivity, capacity, stability, kinetics and manufacturing costs.

The "molecular trapdoor" effect of zeolites was first uncovered by Liu.[11] They demonstrated that for low silica chabazite (Si/Al<3), gas molecules having sufficient ability to induce the temporary deviation of door-keeping cations from the center of 8-rings can be selectively admitted into the nanocages. Based on molecular trapdoor chabazite, they achieved high selectivity for $CO_2/CH_4$ separation (93 at 273 K, 100 kPa) and size-inverse sieving of $CO/N_2$. Moreover, small-pore RHO zeolite was found to have strong cation-dependent structural flexibility and exhibit excellent $CO_2$ adsorption behavior over $N_2$ and $CH_4$ owing to the "trapdoor" effect.[15−17] The cations may locate in the double 8-rings (D8Rs), single 8-rings (S8Rs) and single 6-rings (S6Rs),[9] which can induce framework distortion when dehydration, and decrease the structural symmetry of $Im\bar{3}m$

✉ TIAN Peng
tianpeng@dicp.ac.cn
✉ LIU Zhongmin
liuzm@dicp.ac.cn
1. School of Chemistry, Dalian University of Technology, Dalian 116024, P. R. China;
2. National Engineering Research Center of Lower-Carbon Catalysis Technology, Dalian Institute of Chemical Physics, Chinese Academy of Sciences, Dalian 116023, P. R. China;
3. University of Chinese Academy of Sciences, Beijing 100049, P. R. China


https://doi.org/10.1007/s40242-024-4056-y

to $I\bar{4}3m$ with elliptical 8-rings.[16] Fully exchanged Na-RHO was reported to be the most promising $CO_2$ adsorbent of those studied. Recently, RHO-type SAPO molecular sieve DNL-6 was revealed to be highly efficient for $CO_2$ separation.[10] Na-exchanged DNL-6 exhibited a high separation selectivity for $CO_2/CH_4$ and $CO_2/N_2$.[5]

DNL-6 was first synthesized by our group[18,19] using a hydrothermal method and conventional sources. The development of an environmental-friendly method for the synthesis of DNL-6 would promote its application as an absorbent for $CO_2$ capture. Herein, the spent methanol-to-olefins (MTO) industrial catalyst (with SAPO-34 as the active component) was explored as the main inorganic source for DNL-6 synthesis. It is noted that the olefins production of the MTO units has exceeded 17 Mt/a in China and the corresponding catalyst consumption amounts to about 10000 ton/a.[20] It is highly valuable to convert the spent industrial MTO catalyst into functional materials, which would facilitate the sustainable development of the MTO process. A series of DNL-6 with various silica contents was synthesized and exchanged to Na-DNL-6 with different Na amounts. The prepared materials were explored for the separation of $CO_2/N_2$ and $CO_2/CH_4$. The location of Na cations in Na-DNL-6 was determined by Rietveld refinement to better understand the separation performance.

# 2 Experimental

## 2.1 Materials

The spent industrial MTO catalysts were obtained from commercial DMTO units. Before use for synthesis and characterization, they were calcined at 923 K to remove the carbonaceous deposits. The chemical reagents used for DNL-6 synthesis and ion exchange include diethylamine (DEA, 99.5%, mass fraction), octadecyl trimethyl ammonium bromide (STAB, 99%, mass fraction), phosphoric acid ($H_3PO_4$, 80%, mass fraction), silica sol ($SiO_2$, 27.3%), pseudo-boehmite ($Al_2O_3$, 67.5%, mass fraction), and NaCl (99%). These chemicals were all commercial reagents and used without purification.

## 2.2 Hydrothermal Synthesis

DNL-6 molecular sieves with different silica contents were synthesized with a molar gel ratio of $1.0(Al_2O_3):1.0(P_2O_5):n(SiO_2):0.1(STAB):40(H_2O):2.5(DEA)$ ($n$=0.6, 0.87, 1.2). The synthesis procedure was as follows: the calcined spent MTO catalyst was mixed with deionized water under stirring. Then phosphoric acid, pseudo-boehmite, silica sol, DNL-6 seed (3%, mass fraction, based on dry oxides), STAB, and DEA were added in sequence to the above mixture. After stirring for 30 min, the resulting gel was transferred to a 100 mL stainless steel autoclave and crystallized at 473 K for 24 h under rotation. After crystallization, the solid product was obtained by centrifugation, washing and drying at 373 K. The product was calcined at 832 K for 3 h to remove the organics. The final sample was named D6-$x$ ($x$=0.18, 0.23, 0.28), where $x$ refers to the molar content of $SiO_2$ in DNL-6. The detailed synthesis conditions are given in Table 1.

**Table 1 DNL-6 syntheses, product elemental compositions and solid yields**

| Sample[a] | $x(SiO_2)$/mol | Added amount of inorganic source/g | | | | $m_{sc}/m_t$[b] (%) | Yield (%) | Product composition (in mole) |
|---|---|---|---|---|---|---|---|---|
| | | Spent catalyst | $H_3PO_4$ | $Al_2O_3$ | Si sol | | | |
| D6-0.18 | 0.60 | 6.9 | 9.72 | 2.37 | 0 | 48.8 | 77.8 | $Si_{0.185}Al_{0.500}P_{0.316}O_2$ |
| D6-0.23 | 0.87 | 10.0 | 6.20 | 0 | 0 | 73.5 | 88.4 | $Si_{0.228}Al_{0.499}P_{0.273}O_2$ |
| D6-0.28 | 1.20 | 10.0 | 6.99 | 0 | 3.59 | 66.5 | 64.5 | $Si_{0.281}Al_{0.446}P_{0.273}O_2$ |

*a*. The final gel molar composition for the samples was $2.5DEA:1.0Al_2O_3:1.0P_2O_5:xSiO_2:0.1STAB:40H_2O$ (473 K, 24 h); *b*. $m_{sc}$: the mass of calcined spent catalyst. $m_t$: the total mass of inorganic oxides in the gel.

## 2.3 Ion Exchange

The as-synthesized samples were added to 0.5 mol/L NaCl solution with a solid/liquid ratio of 1 g/20 mL. After exchanging at 333 K for 2 h under stirring, the solid was separated, washed and dried at 373 K. The procedure was repeated 1—7 times depending on the Na amount required. The final sample was named Na$n$-D6-$x$ ($n$=1—7; $x$=0.18, 0.23, 0.28), where $n$ and $x$ refer to the ion exchange cycles and the Si amount in DNL-6, respectively. Prior to the characterization and adsorption tests, the as-synthesized samples were calcined at 823 K for 3 h to remove the organics.

## 2.4 Characterization

The X-ray diffraction (XRD) patterns were obtained on a PANalytical X'Pert PRO X-ray diffractometer using Cu $K\alpha$ radiation ($\lambda$=0.154059 nm) at 40 kV and 40 mA. The scanning electron microscope (SEM) images and EDX mapping were recorded on a Hitachi SU8020 scanning electron microscope. The elemental compositions were measured using a PANalytical AXios X-ray fluorescence (XRF) spectrometer. $N_2$ adsorption-desorption measurements were carried out


https://doi.org/10.1007/s40242-024-4056-y

on a Micromeritics 2020 analyzer at 77 K. Prior to measurement, the sample was degassed at 623 K for at least 5 h. Solid-state NMR experiments were performed on a Bruker Avance NEO 500 (11.7 Tesla) spectrometer. The corresponding resonant frequencies of $^{27}$Al, $^{31}$P and $^{29}$Si are 130.32, 202.46 and 99.35 MHz, respectively. The $^{27}$Al and $^{29}$Si correlation experiments were performed on a 4 mm double resonance probe at 12 kHz, and the $^{31}$P correlation experiments were performed on a 4 mm double resonance probe at 10 kHz. The $^{27}$Al MAS NMR experiment adopted a single pulse program with sampling times of 512, excitation pulse width of 0.35 μs at a small angle (less than π/18), sampling delay of 2 s, $Al(NO_3)_3$ as a chemical shift reference, and calibration to $\delta$ 0. The $^{31}$P MAS NMR experiment adopted a high-power proton decoupling program with 32 sampling times, 1.9 μs pulse width of π/4, 5 s sampling delay, and calibration to $\delta$ 0 using ADP as a chemical shift reference. The $^{29}$Si MAS NMR experiment adopted a high-power proton decoupling procedure with a sampling frequency of 3000—6000, π/4 has a pulse width of 2.9 μs and a sampling delay of 10 s, corrected to $\delta$ −91.5 using kaolin as a chemical shift reference. $NH_3$-TPD was determined on a Micromeritics 2920 chemical adsorption instrument. Prior to the measurement, 0.2 g of calcined samples (40—60 mesh) was loaded and treated at 873 K for 1 h under a He flow. The sample was then reduced to 373 K, and the gas was switched to an $NH_3$-He mixture (containing 2% $NH_3$). After 0.5 h of $NH_3$ adsorption, the sample was further purged by He for 1 h. The $NH_3$-TPD measurement was performed from 373 K to 873 K (10 K/min) under He flow (30 mL/min).

### 2.5 Measurement of $CO_2$, $N_2$ and $CH_4$ Isotherms

Single component adsorption experiments of $N_2$, $CO_2$ and $CH_4$ were conducted by using a Micrometrics ASAP2020. Prior to adsorption measurement, the sample was pretreated at 623 K for 5 h under vacuum ($p/p_0$=$10^{-5}$) to get rid of the adsorbed gas molecules. Adsorption isotherms were measured at 298 K. Adsorption temperature was controlled by condensation pump and Dewar flask with the fluctuations less than ±0.2 K during the experiments. The calculation of separation factor ($\alpha$) was given in the Electronic Supplementary Information (ESI).

### 2.6 Breakthrough Experiments

The breakthrough experiments were performed on the evaluation device shown in Scheme S1 in the ESI. For evaluation, 0.75 g (40—60 mesh) of calcined sample was loaded into a stainless steel tube. The sample was heated to 773 K at a rate of 5 K/min under He and activated at the temperature for 1 h. Afterwards, the temperature was reduced and kept at 298 K by a circulating water bath. The gas was then switched to $CO_2/CH_4$ (50:50, volume ratio) at a flow rate of 3 mL/min or $CO_2/N_2$ (15:85, volume ratio) at a flow rate of 5 mL/min. The effluent gas was analyzed using a mass spectrometer.

Cycling breakthrough experiments were also tested on the apparatus shown in Scheme S1. The test procedure was the same as the above. After each breakthrough experiment, the sample was purged under He flow (20 mL/min) at 373 K for 1 h before the next test.

## 3 Results and Discussion

### 3.1 Synthesis and Characterizations of DNL-6

To get a comprehensive understanding of the composition and properties of the calcined spent catalyst, a variety of characterizations were performed and the corresponding results are presented in Fig. S1 and Table S1 in the ESI. The main components of the catalyst consisting of $Al_2O_3$ (51.0%, mass fraction), $SiO_2$ (26.2%, mass fraction) and $P_2O_5$ (21.4%, mass fraction), which implies that it can simultaneously provide Al, Si and P sources for the synthesis of SAPO molecular sieves. The XRD pattern shows that the spent catalyst has weak diffraction signals associated with the CHA phase, indicating the partial reservation of the SAPO-34 structure (the active component of the MTO catalyst). The SEM image reveals that the spent solid is mainly composed of irregular particles with a wide size distribution (2—30 μm).

Detailed synthesis conditions for DNL-6 by utilization of the calcined spent catalyst are listed in Table 1 and Table S2 in the ESI. The proportion of the spent catalyst in the synthetic gel was in the range of 48%—74% (based on inorganic oxides). The three products with $SiO_2$ molar contents of 0.185, 0.228 and 0.281 are named D6-0.18, D6-0.23 and D6-0.28, respectively. It is noted that higher DEA dosage in the initial gel is important to ensure the product phase purity (Table S2). Otherwise, a small amount of SAPO-34 would appear as an impurity. The synthesis was finished after crystallization at 473 K for 24 h. Further prolonging the crystallization time would lead to a decrease in solid yield. Moreover, it is found that the addition of surfactant STAB is not necessary for the achievement of pure DNL-6, which is different from our previous observations.[18] However, the appearance of surfactant in the gel can help enhance the solid yield (79.1% *vs.* 88.4%).

The powder XRD patterns of the calcined samples are given in Fig. 1A. They are all consistent with that of previously reported DNL-6 with the RHO topology, evidencing the phase purity of the samples. The SEM images shown in Fig. S2 in the ESI indicate that all samples are rhombic dodecahedron crystals in sizes of 0.5—2 μm and no


https://doi.org/10.1007/s40242-024-4056-y

amorphous particles could be observed. $N_2$ sorption isotherms were determined to characterize the textural properties of the calcined samples. From Fig. 1C, they possess a typical type-I isotherm. The corresponding surface areas and micropore volumes are given in Table S3 in the ESI. The values are all comparable with those of the samples synthesized with conventional sources, confirming the high crystallinity of the synthesized materials.

The atomic coordination environments of the as-synthesized DNL-6 were measured by solid-state MAS NMR spectra. As shown in Fig. 2 and Fig. S3 in the ESI, all three $^{31}$P MAS NMR spectra give a strong signal at $\delta$ 28.3, which corresponds to the framework P(4Al) species.[21] In the $^{27}$Al MAS NMR spectra, there was one broad and asymmetric resonance at around $\delta$ 35, which can be assigned to the framework tetrahedral Al species together with a small amount of penta-coordinated Al species formed by coordination with water or template molecules.[22] For $^{29}$Si MAS NMR spectra, DNL-6 samples give resonances at around $\delta$ −91.3, −95.4, −100.0, −104.6 and −109.2, which correspond to the Si(4Al), Si(3Al), Si(2Al), Si(1Al) and Si(0Al) species, respectively. It is clear that following the increase of product silica contents, the Si environments become complicated[23] and the proportion of silica islands increases significantly. The deconvolution results of the $^{29}$Si NMR spectra are displayed in Table S4 in the ESI, showing that the Si(4Al) content decreases from 74.1% for D6-0.18 to 39.0% for D6-0.28.

The $NH_3$-TPD profiles of the calcined samples and the corresponding deconvoluted results are shown in Fig. S4 and Table S5 in the ESI, respectively. The high-temperature desorption band corresponds to the acid sites with moderate/high acid strength, while the low-temperature peak is due to the $NH_3$ desorption from the weak acid sites. Following the increase in product silica contents, the acid amounts show a decreasing trend. Meanwhile, the desorption peak of the moderate and strong acid sites for D6-0.28 moves to a higher temperature, indicating the increased acid strength. This should be resulted from the gradually complex silica environments,[24] as evidenced by the above $^{29}$Si MAS NMR spectra.

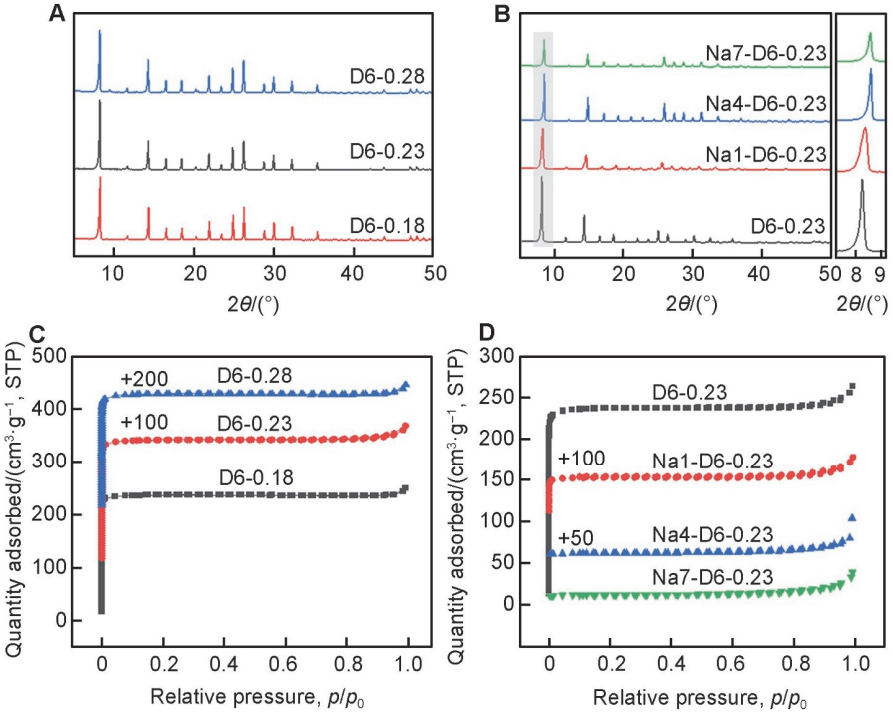


**Fig.1 XRD patterns (A, B) and $N_2$ adsorption-desorption isotherms (C, D) of DNL-6 (A, C) and Na-exchanged DNL-6 (B, D)**

The right figure in (B) is the enlargement of the grey part. The as-synthesized samples are used for (A), and calcined samples are used for (B)—(D).

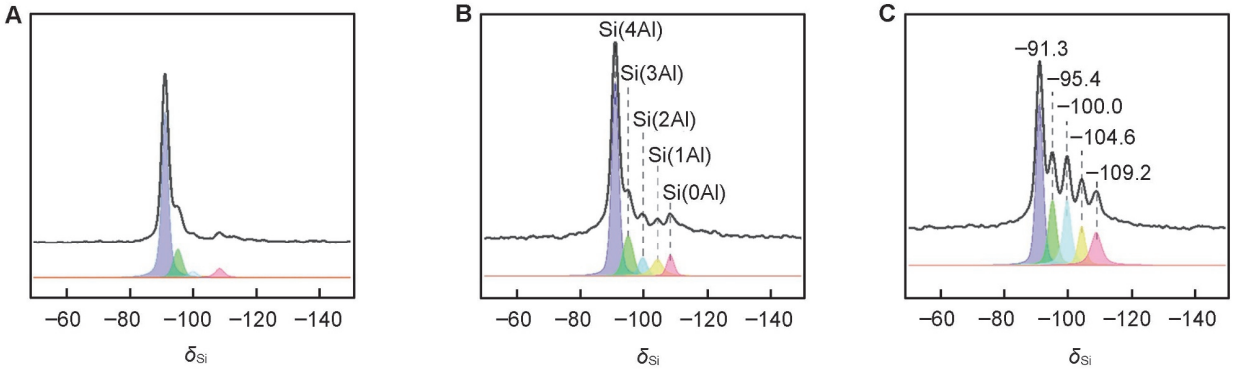


**Fig.2 $^{29}$Si MAS NMR spectra of the as-synthesized DNL-6 samples**

(A) D6-0.18; (B) D6-0.23; (C) D6-0.28.


https://doi.org/10.1007/s40242-024-4056-y

### 3.2 Preparation and Characterizations of Na-DNL-6

A serial of Na-exchanged DNL-6 was prepared by direct ion exchange method using the as-synthesized DNL-6 as a precursor. This method was first reported by us for the preparation of Cu/SAPO-34,[25] which can simplify the exchange procedure and avoid structural decay of SAPO molecular sieves during ion exchange. The obtained samples were named Na*n*-D6-*x*, where *n* and *x* refer to exchange cycles and product silica content, respectively. From Fig. S5 in the ESI, the Na/Si molar ratio of the samples increases gradually with the incremental exchange cycles, but the slope slows down at higher cycles. Under the same ion exchange cycle, D6-0.18 and D6-0.23 have comparable Na/Si ratios, which are obviously higher than that of D6-0.28. This should be owing to the higher amount of Si islands in the latter sample, causing lower exchangeable sites. The Na/Si molar ratio can reach as high as 71% for Na7-D6-0.23 after 7 exchange cycles, which is close to the saturated exchange capacity (79.5%) of the sample calculated based on the $^{29}$Si MAS NMR result. Fig. S6 in the ESI shows the SEM and elemental mapping images of the calcined Na-exchanged samples, which confirm their well retained morphology and homogenous distribution of Na in crystals. The thermal analysis results are displayed in Fig. S7 and Table S6 in the ESI. The organics content shows a gradual decrease from D6-0.23 (23.2%) to Na4-D6-0.23 (4.7%) to Na7-D6-0.23 (2.8%), implying the expelling of organotemplate following the incorporation of Na cations.

The XRD patterns and $N_2$ sorption results of the calcined Na-DNL-6 samples are shown in Fig. 1, Fig. S8 and Table S3 in the ESI. Compared with the XRD patterns of the precursors, a gradual shift to the high degree can be observed following the increase of exchange cycles. Meanwhile, the $N_2$ adsorption capacity shows a significant decrease. The phenomena should be caused by the incorporation of Na cations, leading to structural distortion and contraction of unit cell.[5,26,27]

### 3.3 Structure of Dehydrated Na-DNL-6

The structure of the calcined Na-exchanged DNL-6 was determined by Rietveld refinement against PXRD data. The details for crystallographic analysis are given in the ESI. Here, Na7-D6-0.23 with a relatively high Na content was chosen for refinement analysis. As precious works have revealed the distorted crystallographic structures of metal-exchanged zeolite Rho and DNL-6, a distorted RHO structural model, including the initial atom coordinates (P, Al, four O atoms) in the asymmetric units, was built based on our previous work.[5] The crystallographic details of Rietveld refinement are listed in Table S7 in the ESI. After framework optimization, the space group changes from highly symmetric $I\bar{4}3m$ to $I23$ with lower symmetry. From Fig.3, Table S8 and Table S9 in the ESI, most of Na cations (average 5.66 Na per unit cell) are sited in the center of S8R, and the framework O atoms distort the 8-rings to a certain extent in order to better cooperate with Na cations. Meanwhile, small fraction of Na cations locates in the center of S6Rs (average 1.74 Na per unit cell).

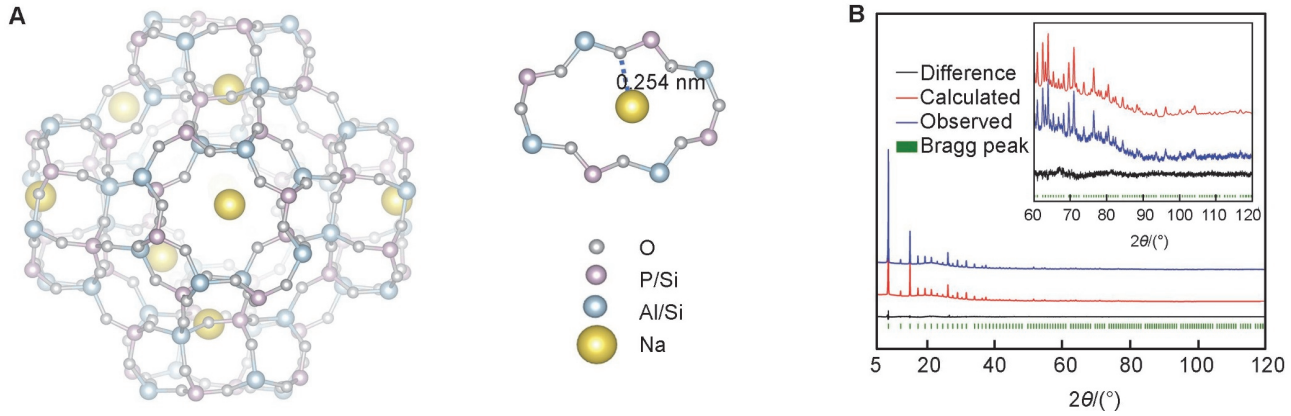


**Fig. 3 Crystallographic structure of Na7-D6-0.23 (A) and the corresponding final Rietveld refinement plots (B)**
The blue, red and black curves are the observed, calculated and difference patterns, respectively. The green bars show the positions of Bragg positions.

### 3.4 $CO_2$, $N_2$ and $CH_4$ Adsorption Isotherms

The adsorption isotherms of the calcined H-type DNL-6 for $CO_2$, $N_2$ and $CH_4$ were measured at 298 K between 0 and 101 kPa. As shown in Fig. 4, Fig. S9 in the ESI and Table 1, all samples show much higher uptake of $CO_2$ than those of $N_2$ and $CH_4$, which should be owing to the strong quadrupolar interactions of $CO_2$ with adsorption sites.[28] The uptake of


https://doi.org/10.1007/s40242-024-4056-y

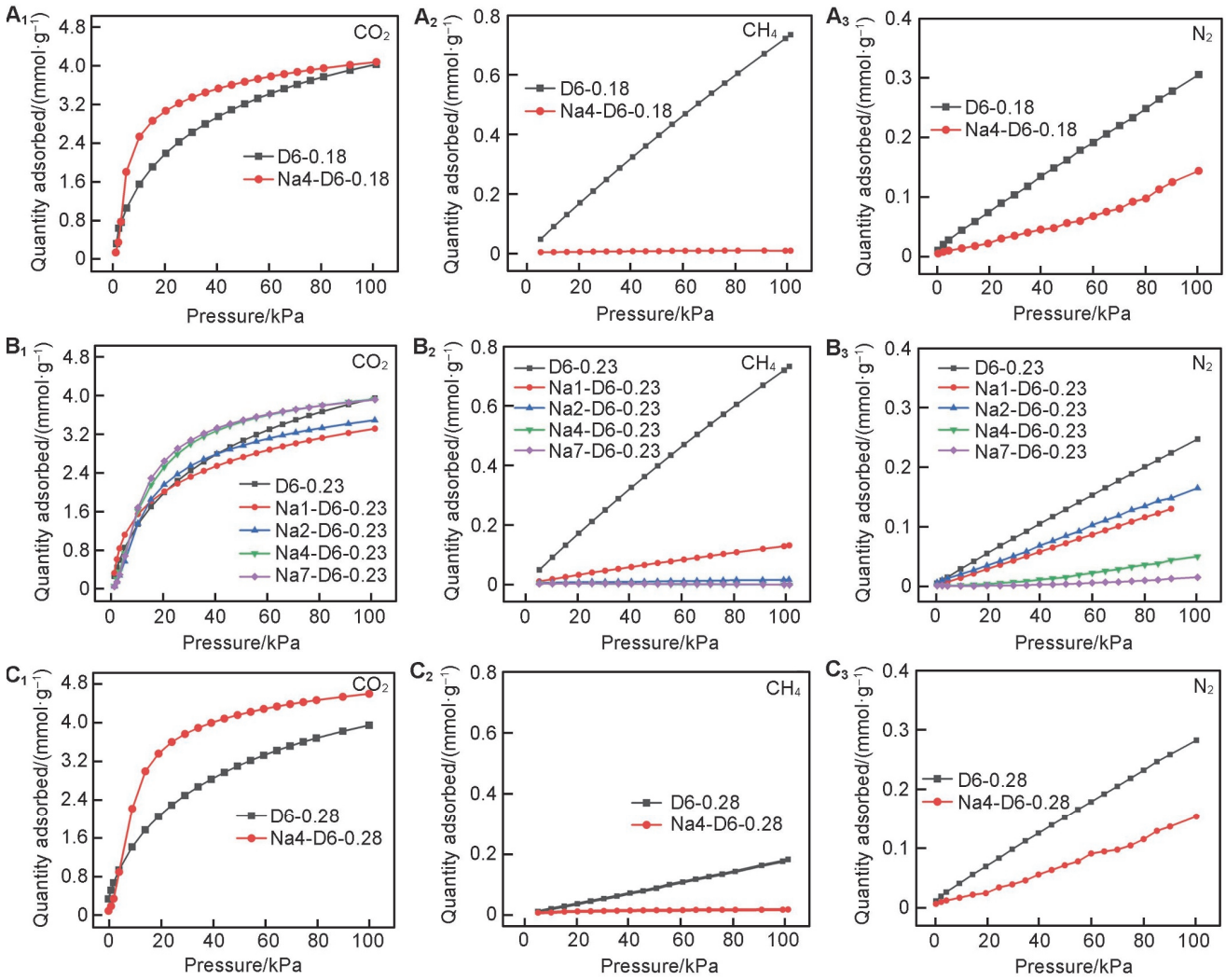


**Fig. 4 Adsorption isotherms of $CO_2$ ($A_1$, $B_1$, $C_1$), $N_2$ ($A_2$, $B_2$, $C_2$) and $CH_4$, ($A_3$, $B_3$, $C_3$), on DNL-6 before and after Na exchange at 298 K between 0 and 101 kPa**

($A_1$—$A_3$) D6-0.18 and Na4-D6-0.18; ($B_1$—$B_3$) D6-0.23 and Na*n*-D6-0.23 (*n*=1, 2, 4, 7); ($C_1$—$C_3$) D6-0.28 and Na4-D6-0.28.

$CO_2$ at 298 K and 101 kPa has an order of D6-0.18 (4.03 mmol/g)>D6-0.23 (3.98 mmol/g)>D6-0.28 (3.92 mmol/g). As previous works have demonstrated that the Brønsted acid sites of molecular sieves were preferential adsorption sites for $CO_2$,[29−31] the gradually decreased acid amounts from D6-0.18 to D6-0.28 revealed by $NH_3$-TPD explain well the above observed sequence. The separation factor ($\alpha$) of $CO_2/N_2$ (0.15/0.85 kPa) and $CO_2/CH_4$ (0.5/0.5 kPa), calculated based on the single component isotherms, is shown in Table 2. The three samples possess comparable $CO_2/N_2$ separation selectivity (41—47). For $CO_2/CH_4$ separation, D6-0.28 shows higher separation factor of 34 than D6-0.18 and D6-0.23. This is due to the low $CH_4$ uptake on D6-0.28, likely caused by the relatively large size of $CH_4$ and the slightly structural distortion of DNL-6 due to the formation of large amount of Si islands.

To evaluate the adsorption performance of Na-exchanged DNL-6, Na4-D6-*x* samples were first investigated and the adsorption isotherms are displayed in Fig. 4. The $CO_2$ uptakes of the samples at 298 K and 101 kPa are comparable to their corresponding H-type precursors or even higher. Moreover, obviously higher $CO_2$ uptakes at low pressure region can be observed, which should be resulted from the strong interactions between $CO_2$ and Na cations. The $N_2$ uptakes of Na-exchanged samples show a clear drop as compared with that of H-type DNL-6, and nearly no $CH_4$ uptakes occur. The decreased uptakes of $N_2$ and $CH_4$ thus lead to a sharp increase in separation selectivity. From Table 2, Na4-D6-0.23 possesses the highest separation factor for $CO_2/N_2$ (1229) and $CO_2/CH_4$ (∞) among the Na4-D6-*x* samples. Both the $CO_2$ uptake and separation selectivity on Na4-D6-0.23 are even better than those on Na-DNL-6 synthesized by using conventional raw sources.[5]

Given the high separation selectivity achieved on Na4-D6-0.23, Na*n*-D6-0.23 samples with different Na exchange degrees were further explored for gas adsorption. From


https://doi.org/10.1007/s40242-024-4056-y

**Table 2 Comparison of equilibrium $CO_2$ uptake and selectivity on the samples**

| Sample | Uptake of $CO_2$/(mmol·g$^{-1}$) | | | Uptake of $N_2$/(mmol·g$^{-1}$) | | Uptake of $CH_4$/(mmol·g$^{-1}$) | | $\alpha(CO_2/N_2)$ | $\alpha(CO_2/CH_4)$ |
|---|---|---|---|---|---|---|---|---|---|
| | 15 kPa | 50 kPa | 101 kPa | 85 kPa | 101 kPa | 50 kPa | 101 kPa | (15/85 kPa) | (50/50 kPa) |
| D6-0.18 | 1.91 | 3.33 | 4.03 | 0.26 | 0.31 | 0.40 | 0.74 | 41 | 8 |
| Na4-D6-0.18 | 2.86 | 3.67 | 4.08 | 0.11 | 0.14 | 0.0078 | 0 | 147 | 470 |
| D6-0.23 | 1.73 | 3.10 | 3.98 | 0.21 | 0.25 | 0.40 | 0.74 | 47 | 8 |
| Na1-D6-0.23 | 1.85 | 2.76 | 3.35 | 0.12 | 0.12 | 0.07 | 0.13 | 87 | 39 |
| Na2-D6-0.23 | 1.88 | 3.00 | 3.52 | 0.14 | 0.16 | 0.0094 | 0.02 | 76 | 318 |
| Na4-D6-0.23 | 2.82 | 3.66 | 3.97 | 0.013 | 0.02 | 0 | 0 | 1229 | ∞ |
| Na7-D6-0.23 | 2.32 | 3.52 | 3.95 | 0.0096 | 0.01 | 0 | 0 | 1369 | ∞ |
| D6-0.28 | 2.02 | 3.07 | 3.92 | 0.25 | 0.28 | 0.09 | 0.18 | 46 | 34 |
| Na4-D6-0.28 | 2.96 | 4.13 | 4.57 | 0.13 | 0.15 | 0.017 | 0.02 | 129 | 243 |

Table 2, following the increase of Na amount, the $CO_2$ uptake at 298 K and 101 kPa shows a first decrease and then recovery, while the uptakes of $N_2$ and $CH_4$ display a monotonous drop to about zero, which results in significantly increased separation selectivity. The highest separation factor of 1369 for $CO_2/N_2$ can be observed on Na7-D6-0.23. More interestingly, the separation factor of $CO_2/CH_4$ becomes infinity on Na4-D6-0.23 and Na7-D6-0.23. These results suggest that Na-exchanged DNL-6 is a promising candidate for $CO_2$ separation.

According to the literatures[26,27,32,33] and the above structural refinement results, the unaffected $CO_2$ uptake on Na-exchanged DNL-6 and the improved separation selectivity for $CO_2/N_2$ and $CO_2/CH_4$ can be understood as follows. $CO_2$ molecules with high quadrupole moment have strong interactions with Na cations, which can induce the temporary movement of Na cations away from the center of S8Rs and thus allow the admission of $CO_2$. This is the so-called "trapdoor" effect. However, for $N_2$ and $CH_4$, their larger kinetic diameters ($N_2$ 0.36 nm, $CH_4$ 0.38 nm, $CO_2$ 0.33 nm) and weak interactions with Na cations make them difficult in pushing away Na cations, inhibiting their entrance. Moreover, previous work[5] revealed that the interactions between Na cations and the S8Rs in DNL-6 were stronger than those in RHO zeolite, which led to an enhanced "trapdoor" effect. This agrees well with the observed superior separation behavior of Na-DNL-6.

### 3.5 Breakthrough Experiments

The breakthrough experiments were carried out at 298 K and atmospheric pressure to determine the dynamic adsorption and separation performance of Na4-D6-0.23 by utilizing binary $CO_2/CH_4$ (50:50, volume ratio) and $CO_2/N_2$ (15:85, volume ratio) gas mixtures.[34,35] As shown in Fig. S10 in the ESI, both $N_2$ and $CH_4$ penetrated quickly as the gas mixtures were passing through the adsorbent, while $CO_2$ was retained until the adsorbent was saturated. This evidences that Na4-D6-0.23 has a stronger affinity for $CO_2$ than for $N_2$ and $CH_4$, in consistence with the above observed high adsorption equilibrium selectivity for $CO_2/CH_4$ and $CO_2/N_2$. The dynamic separation selectivity is calculated to be 435 for $CO_2/CH_4$ and 150 for $CO_2/N_2$. Although the values are lower than those from the pure component adsorption isotherms, Na-type DNL-6 can be regarded as one of the highly selective adsorbents under dynamic conditions. Consecutive breakthrough experiments were further performed to learn the regeneration capability of Na4-D6-0.23. As shown in Fig. S11 in the ESI, the experiments were repeated for five cycles. Na4-D6-0.23 can restore its original $CO_2$ adsorption capacity after regeneration and maintain the high separation selectivity.

## 4 Conclusions

In summary, DNL-6 molecular sieves with various silica contents were synthesized by utilization of spent industrial MTO catalyst as the main inorganic source. Na cations were introduced into DNL-6 by ion exchange using the as-synthesized DNL-6 as a precursor. During ion exchange, the template molecules were found to leave away from the crystals following the incorporation of Na cations. Rietveld refinement demonstrates that Na cations in calcined Na-DNL-6 are mainly located in the S8Rs. Adsorption studies indicate that following the increase of Na exchange degree, the $CO_2$ uptake of Na-DNL-6 first shows a increase and then recovery to be comparable with that of H-DNL-6, while the uptakes of $CH_4$ and $N_2$ drop to near zero. Na-DNL-6 with a high Na exchange degree possessed superior separation selectivity for $CO_2/CH_4$ and $CO_2/N_2$, which arise from the "trapdoor" effect associated with the Na cations sited in the S8Rs. Both selectivity values are at the top level of zeolitic adsorbents. Breakthrough experiments further demonstrated that Na-DNL-6 can effectively separate $CO_2$ from $N_2$ and $CH_4$.


https://doi.org/10.1007/s40242-024-4056-y

## Electronic Supplementary Information

Supplementary material is available in the online version of this article at http://dx.doi.org/10.1007/s40242-024-4056-y.

## Acknowledgements

This work was supported by the National Natural Science Foundation of China (Nos. 21991090, 21991091, 22171259, 22272173) and the AI S&T Program of Yulin Branch, Dalian National Laboratory for Clean Energy, CAS (No. DNL-YL A202206).
The authors thank to the funding from the Sino-French IRN (International Research Network).

## Conflicts of Interest

The authors declare no conflicts of interest.

## References

[1] Gilfillan D., Marland G., *Earth Syst. Sci. Data*, **2020**, *2020*, 1.
[2] Liu R. S., Xu S., Hao G. P., Lu A. H., *Chem. Res. Chinese Universities*, **2022**, *38*, 18.
[3] Zhang P., Zhang C., Wang L., Dong J., Gai D., Wang W., Nguyen T. S., Yavuz C. T., Zou X., Zhu G., *Adv. Funct. Mater.*, **2023**, *33*, 2210091.
[4] Sahoo R., Mondal S., Mukherjee D., Das M. C., *Adv. Funct. Mater.*, **2022**, *32*, 2207197.
[5] Wang X., Yan N., Xie M., Liu P., Bai P., Su H., Wang B., Wang Y., Li L., Cheng T., *Chem. Sci.*, **2021**, *12*, 8803.
[6] Agrawal M., Sholl D. S., *ACS Appl. Mater. Interfaces*, **2019**, *11*, 31060.
[7] Zhou Y., Zhang J., Wang L., Cui X., Liu X., Wong S. S., An H., Yan N., Xie J., Yu C., *Science*, **2021**, *373*, 315.
[8] Liang J., Nuhnen A., Millan S., Breitzke H., Gvilava V., Buntkowsky G., Janiak C., *Angew. Chem. Int. Ed.*, **2020**, *59*, 6068.
[9] Altundal O. F., Altintas C., Keskin S., *J. Mater. Chem.*, **2020**, *8*, 14609.
[10] Liu Y., Wang S., Meng X., Ye Y., Song X., Liang Z. , Zhao Y., *Angew. Chem. Int. Ed.*, **2020**, *59*, 19487.
[11] Shang J., Li G., Singh R., Gu Q., Nairn K. M., Bastow T. J., Medhekar N., Doherty C. M., Hill A. J., Liu J. Z., *J. Am. Chem. Soc.*, **2012**, *134*, 19246.
[12] F. Duan, X. Liu, D. Qu, B. Li L., Wu, *CCS Chemistry*, **2021**, *3*, 2676.
[13] Zhang X., Wang Z., Chen Z., Zhu Y., Liu Z., Li F., Zhou W., Dong Z., Fan J., Liu L., *Appl. Catal. B*: *Environ.*, **2022**, *317*, 121771.
[14] Choi H. J., Jo D., Min J. G., Hong S. B., *Angew. Chem. Int. Ed.*, **2021**, *60*, 4307.
[15] Zhao J., Mousavi S. H., Xiao G., Mokarizadeh A. H., Moore T., Chen K., Gu Q., Singh R., Zavabeti A., Liu J. Z., *J. Am. Chem. Soc.*, **2021**, *143*, 15195.
[16] Balestra S. R., Hamad S., Ruiz-Salvador A. R., Domínguez-García V., Merkling P. J., Dubbeldam D., Calero S., *Chem. Mat.*, **2015**, *27*, 5657.
[17] Georgieva V. M., Bruce E. L., Verbraeken M. C., Scott A. R., Casteel Jr W. J., Brandani S., Wright P. A., *J. Am. Chem. Soc.*, **2019**, *141*, 12744.
[18] Su X., Tian P., Li J., Zhang Y., Meng S., He Y., Fan D., Liu Z., *Microporous Mesoporous Mat.*, **2011**, *144*, 113.
[19] Yang M., Tian P., Liu L., Wang C., Xu S., He Y., Liu Z., *CrystEngComm.*, **2015**, *17*, 8555.
[20] Liu Z., Wang Q., Liu S., Yang M., Fan D., Zhu D., Tian P., *Mater. Today Sustain.*, **2023**, *21*, 100302.
[21] Huang Y., Machado D., Kirby C. W., *J. Phys. Chem. B*, **2004**, *108*, 1855.
[22] Blackwell C., Patton R., *J. Phys. Chem.*, **1988**, *92*, 3965.
[23] Tan J., Liu Z., Bao X., Liu X., Han X., He C., Zhai R., *Microporous Mesoporous Mat.*, **2002**, *53*, 97.
[24] Rodríguez-González L., Hermes F., Bertmer M., Rodríguez-Castellón E., Jiménez-López A., Simon U., *Appl. Catal. A*: *Gen.*, **2007**, *328*, 174.
[25] Xiang X., Yang M., Gao B., Qiao Y., Tian P., Xu S., Liu Z., *RSC Adv.*, **2016**, *6*, 12544.
[26] Lozinska M. M., Mangano E., Mowat J. P., Shepherd A. M., Howe R. F., Thompson S. P., Parker J. E., Brandani S., Wright P. A., *J. Am. Chem. Soc.*, **2012**, *134*, 17628.
[27] Lozinska M. M., Mowat J. P., Wright P. A., Thompson S. P., Jorda J. L., Palomino M., Valencia S., Rey F., *Chem. Mat.*, **2014**, *26*, 2052.
[28] Harlick P. J., Tezel F. H., *Microporous Mesoporous Mat.*, **2004**, *76*, 71.
[29] Deroche I., Gaberova L., Maurin G., Castro M., Wright P., Llewellyn P., *J. Phys. Chem.*, **2008**, *112*, 5048.
[30] Li Y., Chen H., Wang C., Ye Y., Li L., Song X.,Yu J., *Chem. Sci.*, **2022**, *13*, 5687.
[31] Wang D., Tian P., Yang M., Xu S., Fan D., Su X., Yang Y., Wang C., Liu Z., *Microporous Mesoporous Mat.*, **2014**, *194*, 8.
[32] Reisner B. A., Lee Y., Hanson J. C., Jones G. A., Parise J. B., Corbin D. R., Toby B. H., Freitag A., Larese J. Z., Kahlenberg V., *Chem. Commun.*, **2000**, *22*, 2221.
[33] Ke Q., Sun T., Wei X., Guo Y., Xu S., Wang S., *Chem. Eng. J.*, **2019**, *359*, 344.
[34] Bower J. K., Barpaga D., Prodinger S., Krishna R., Schaef H. T., McGrail B. P., Derewinski M. A., Motkuri R. K., *ACS Appl. Mater*, **2018**, *10*, 14287.
[35] Wang S., Bai P., Sun M., Liu W., Li D., Wu W., Yan W., Shang J., Yu J., *Adv. Sci.*, **2019**, *6*, 1901317.